Enhancing Noise Robustness in SiN Microring Photonic Reservoirs Enabled by 2D Material Nonlinearities

Sanika Inamdar[1], Lalit Singh[1*✉], Sholehin Juperi[1], Gokul Jayakumar[1], Wenyu Jiang[2], Lydie Ferrier[3], Sang Hoon Chae[1,4,5✉]*

[1]School of Electrical and Electronic Engineering, Nanyang Technological University, Singapore, 639798, Singapore.

[2]Institute for Infocomm Research, Agency for Science, Technology and Research (A*STAR), Singapore

[3]Ecole Centrale de Lyon, INSA Lyon, Université Claude Bernard Lyon 1, CPE Lyon, CNRS, INL, UMR5270, Ecully, 69130 France.

[4]School of Materials Science and Engineering, Nanyang Technological University, Singapore, 639798, Singapore.

[5]CNRS-International-NTU-Thales Research Alliance (CINTRA), IRL 3288, 50 Nanyang Drive, Singapore, 637553, Singapore.

[*]These authors contributed equally.

✉*e-mail:* lalit.singh@ntu.edu.sg, sanghoon.chae@ntu.edu.sg

Abstract

Photonic reservoir computing offers a promising route toward ultrafast, low-energy temporal signal processing, but its performance is intrinsically limited by the nonlinear characteristics and noise of its nodes. Conventional silicon microring reservoirs suffer from high optical loss and thermo-optic fluctuations, which raise the normalized mean-square error (NMSE) and reduce the signal-to-noise ratio (SNR). While silicon nitride (SiN) mitigates optical losses, it has the weakness of lacking inherent nonlinearity and bistability. Here, we incorporate with a monolayer of WSe_2 onto SiN microring (MRR) to enhance the third-order susceptibility, resulting in a sharper resonance response and a deeper bistable potential. This hybrid integration improves dynamic stability against noise, suppresses unwanted resonance drift, and enhances the noise robustness. The WSe_2-SiN MRR

reservoirs achieve a 4 dB increase in SNR and a 30% reduction in NMSE. By integrating with 2D material layers, training accuracy reaches ~94% in 30–40 iterations, which is over five times faster than the bare SiN counterpart. We evaluated time-series prediction using the NARMA-10 and NARMA-20 benchmarks. Both simulations and experiments confirm robust hysteresis, longer memory retention, and stable operation exceeding 5,000 cycles, highlighting a practical pathway toward noise-tolerant, energy-efficient photonic reservoirs for high-speed edge computing and signal prediction.

Keywords

Nonlinearity and Bistability**,** Noise resilience, Time-Series Prediction, WSe_2

Introduction

The explosive growth of data in modern information systems has increased the demand for fast and efficient learning algorithms. Reservoir computing (RC), a recurrent neural network architecture, provides a powerful means for processing temporal and sequential data[1–4]. Owing to its efficient training process, it emerged as a promising platform for real-time computation[5–7]. Photonic implementations of reservoir computing take these advantages further by exploiting the intrinsic parallelism, broad optical bandwidth, and ultrafast response of photonic devices. Such photonic RC bridges machine learning and photonics for edge-AI applications[5,8–10]. A randomly weighted inputs pass through a nonlinear reservoir, while only the output layer is trained, enabling fast and energy efficient operation.

Among various platforms, microring resonators (MRRs) provide a compact and scalable solution for photonic RC, where optical feedback and refractive-index-driven nonlinearity generate the complex dynamics required for computation[11]. Nonlinearity and bistability are crucial to reservoir computing[12,13]. Nonlinearity enhances computing accuracy by keeping reservoir stable. When thermal or other external noise push the resonance away from its operating point, the nonlinear change in the refractive index shifts it back toward desired resonance wavelength[14–17]. Bistability introduces short-term memory through hysteresis, allowing the system to retain information from past inputs and maintain stable operation under fluctuating conditions[16–20].

Conventional silicon-based MRR reservoirs suffer from high propagation loss and introduces noise due to large thermo-optic coefficient and free carrier effects, which increases normalize mean square error (NMSE), suppress Signal to noise Ratio (SNR), and hence degraded photonic RC performance. Silicon nitride (SiN) provides ultra-low optical loss and a high-Q platform with negligible thermal and carrier-related fluctuations, making it far more stable[11]. However, its weak third-order susceptibility (χ^3) and limited bistability restrict nonlinear state separation and noise tolerance, often yielding shallow dynamic responses[18,21]. Integrating atomically thin transition metal dichalcogenides (TMDs) such as WSe_2 into SiN can introduces strong nonlinearity without introducing optical absorption due to their large bandgaps at 1550 nm[22–24]. SiN microring with such heterogeneously integrated materials enhance χ^3 driven bistability in MRR and improves noise resilience for accurate time-series prediction in reservoir computing and related tasks[25–29].

To overcome the intrinsic trade-off between low loss and weak nonlinearity in SiN photonics, here we proposed a hybrid microring resonator that heterogenous integrates a monolayer of WSe_2 atop SiN, achieving strong χ^3 and optical bistability while preserving SiN's low-loss and high-Q. Device with 2D integration reveal a pronounced enhancement in nonlinear response, with bistability emerging at lower optical powers. The WSe_2-SiN MRR reservoirs achieve a 4 dB increase in signal-to-noise ratio (SNR) and a 30% reduction in normalized mean-square error. Integration with the 2D layer accelerates training, achieving 94% accuracy with more than 5 times faster speed compared to the bare SiN counterpart. To further benchmark time-series prediction we evaluated using the NARMA-10 and NARMA-20. Both simulations and experiments demonstrate robust hysteresis and stable operation exceeding 5,000 cycles. Such stability and noise tolerance position the WSe_2-SiN microring as a practical core for integrated photonic processors in edge AI, adaptive control, and real-time signal prediction.

Photonic Reservoir Computing for time series prediction

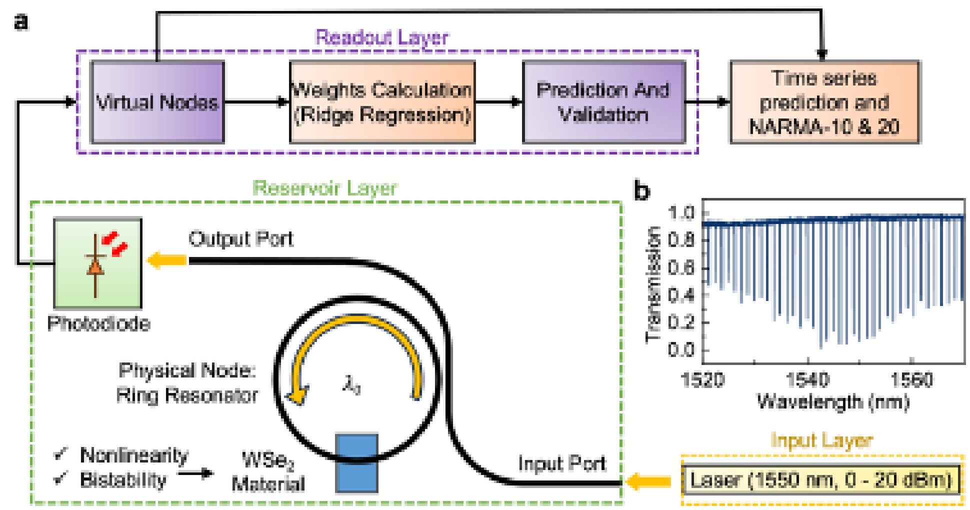

Figure 1. Schematic overview of the proposed photonic reservoir computing system integrated with 2D materials. (a) Schematic of the overall architecture comprising the input layer (laser source), reservoir layer (microring resonator integrated with a 2D material), and readout layer (ridge regression-based weight optimization, prediction, and validation). The reservoir exploits carrier dynamics in the 2D material to enhance optical nonlinearity and introduce bistability. (b) Simulated transmission spectrum of the microring resonator showing multiple resonance dips across the C-band.

RC is a bio-inspired learning framework consisting of a recurrent neural network, whose internal connections are random and fixed over time. It consists of three functional layers: the input layer, the reservoir layer, and the readout layer. The input signal drives the dynamic evolution of the reservoir's internal nodes, while the output is obtained through a linear readout of their collective states. Figure 1a shows the block diagram of the proposed SiN microring-based reservoir computing. In the input layer, a tunable CW laser (1510–1600 nm) is coupled into the MRR input port with variable input power (0–20 dBm). Within the reservoir layer, the input is transformed by the physical node's nonlinear, memory-bearing dynamics. The SiN microring resonator acts as the reservoir node, while a monolayer of WSe_2 integrated on its surface provides strong third-order nonlinearity (χ^3) and optical bistability. The proposed noise-robust mechanism can be extended to other 2D materials, provided they exhibit a strong third-order nonlinear response (high χ^3 value) without introducing significant optical loss. The enhanced nonlinearity introduced by WSe_2 enriches the system's dynamic response and improves robustness against noise fluctuations. The output from the physical node is detected by a photodiode and subsequently processed in the readout layer. In the readout layer, the delayed virtual-node states x(t) are linearly combined to produce the output $\hat{y}(t)=W^T x(t)$, where the weight vector W is optimized using ridge regression for time-series prediction. The time series u(t) and target y(t) = u(t+1), which is a future prediction, the model learns from past inputs and predicts the future time series parameters. After training, the reservoir's predictive performance is evaluated using the NARMA-10 and NARMA-20 benchmarks standard tests in reservoir computing that assess memory capacity, nonlinearity, and noise robustness. These tasks require the system to forecast future outputs from a sequence of past inputs and responses, emulating real-world time-series prediction. Such evaluations are widely used across communication networks, financial analytics, industrial IoT, and autonomous edge-AI applications. The transmission spectrum shown in Figure 1b corresponds to the optical output measured from the output port of the fabricated microring resonator. The spectrum was recorded experimentally by sweeping the input wavelength from 1520 nm to 1580 nm at an input power of 0 dBm, revealing a series of well-defined resonance dips that characterize the ring's spectral response.

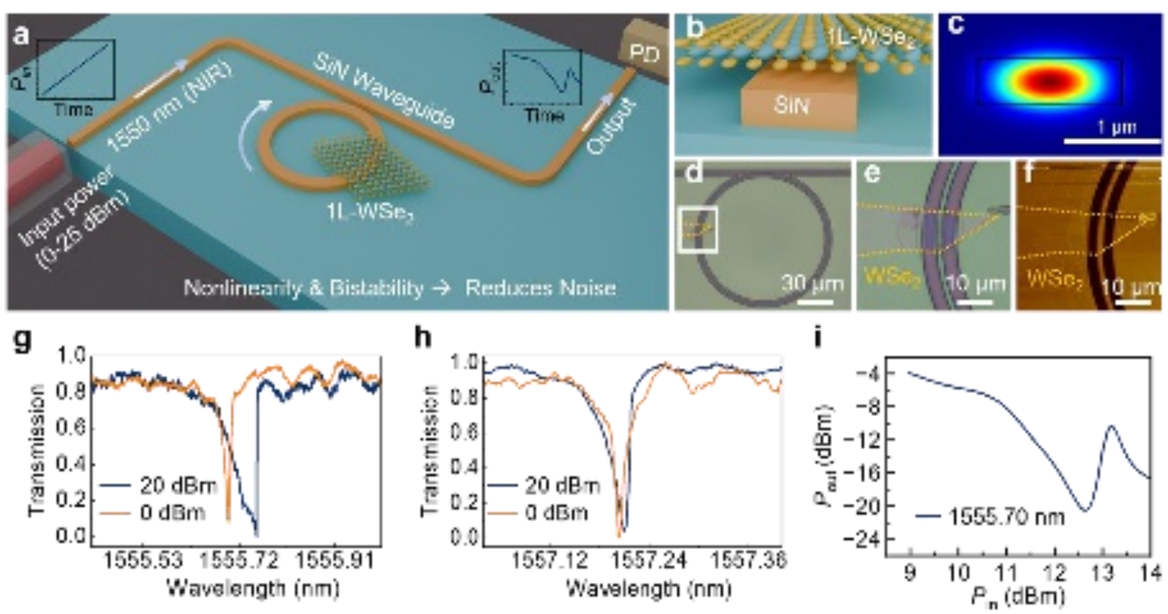

Figure 2. Experimental confirmation of optical nonlinearity and bistability in a microring resonator. (a) Schematic of the fabricated SiN microring resonator (MRR) with an integrated 2D material, a tunable laser with input power varied from 0 to 20 dBm. (b) Cross-sectional schematic of a SiN microring resonator integrated with a monolayer of WSe_2. (c) Simulated optical mode profile of the corresponding waveguide structure. (d) Optical microscope image of the fabricated SiN microring resonator integrated with a monolayer of WSe_2. (e) Magnified optical image showing the transferred monolayer WSe_2 region on the microring. (f) Atomic force microscopy (AFM) image confirming the

monolayer thickness of WSe_2 on the resonator. (g) Transmission spectra measured under varying input powers, showing clear optical bistable behaviour induced by the integration of the 2D WSe_2. (h) Comparative transmission spectra of the microring without the 2D layer, illustrating the absence of bistability. (i) Input and output power relationship, P_{in} and P_{out} highlighting the nonlinear hysteresis loop characteristic of optical bistability.

Figure 2 summarizes the design, fabrication, and experimental confirmation of optical nonlinearity and bistability in the WSe_2-SiN microring resonator. A schematic of the device and measurement setup is shown in Figure 2a, where a tunable laser (1510–1600 nm) with adjustable input power (0–20 dBm) is coupled into the bus waveguide. The microring comprises a high-Q SiN cavity partially covered with a monolayer of WSe_2, as illustrated in the cross-sectional schematic (Figure 2b) and simulated optical mode profile of single mode (Figure 2c). The waveguide has a width of 1.2 µm and a thickness of 350 nm. Optical and AFM images (Figures 2d–f) confirm the precise transfer of a uniform WSe_2 monolayer on the resonator surface. The measured transmission spectra (Figure 2g) show a pronounced power-dependent resonance shift, evidencing optical bistability induced by the strong χ^3 nonlinearity of WSe_2. In contrast, the reference SiN ring without 2D integration (Figure 2h) exhibits linear transmission with no bistable behavior for same input power. The input-output power relation (Figure 2i) further reveals the characteristic nonlinear hysteresis, confirming that the bistability originates from the enhanced nonlinearity rather than thermal effects.

In the WSe_2-SiN microring, the nonlinearity of WSe_2 introduces intensity-dependent refractive-index change. The enhanced optical nonlinearity introduced by the WSe_2 layer enables bistable operation in the microring. The strong χ^3 response of WSe_2 introduces a self-regulating feedback mechanism[19,20,28,30,31]. When the intracavity power increases, WSe_2 slightly shifts the effective index so that the resonance moves opposite to the thermal drift produced in SiN. This prevents the cavity from drifting uncontrollably and keeps the system in a balanced state. As the input power rises, the device first heats through SiN's thermo-optic effect, pushing the resonance away and reducing the stored power. As the cavity cools, the WSe_2 nonlinearity strengthens again, raising the intensity. This push–pull interaction between the thermal shift in SiN and the nonlinearity in WSe_2 naturally leads to stable bistability. Bistability is a fundamental aspect of the reservoir's operation, rather than merely a performance enhancement. Bare SiN alone requires significantly higher input power to reach comparable bistability, whereas with the integration of 2D layer lowers the threshold power.

Analysis: with and without WSe_2

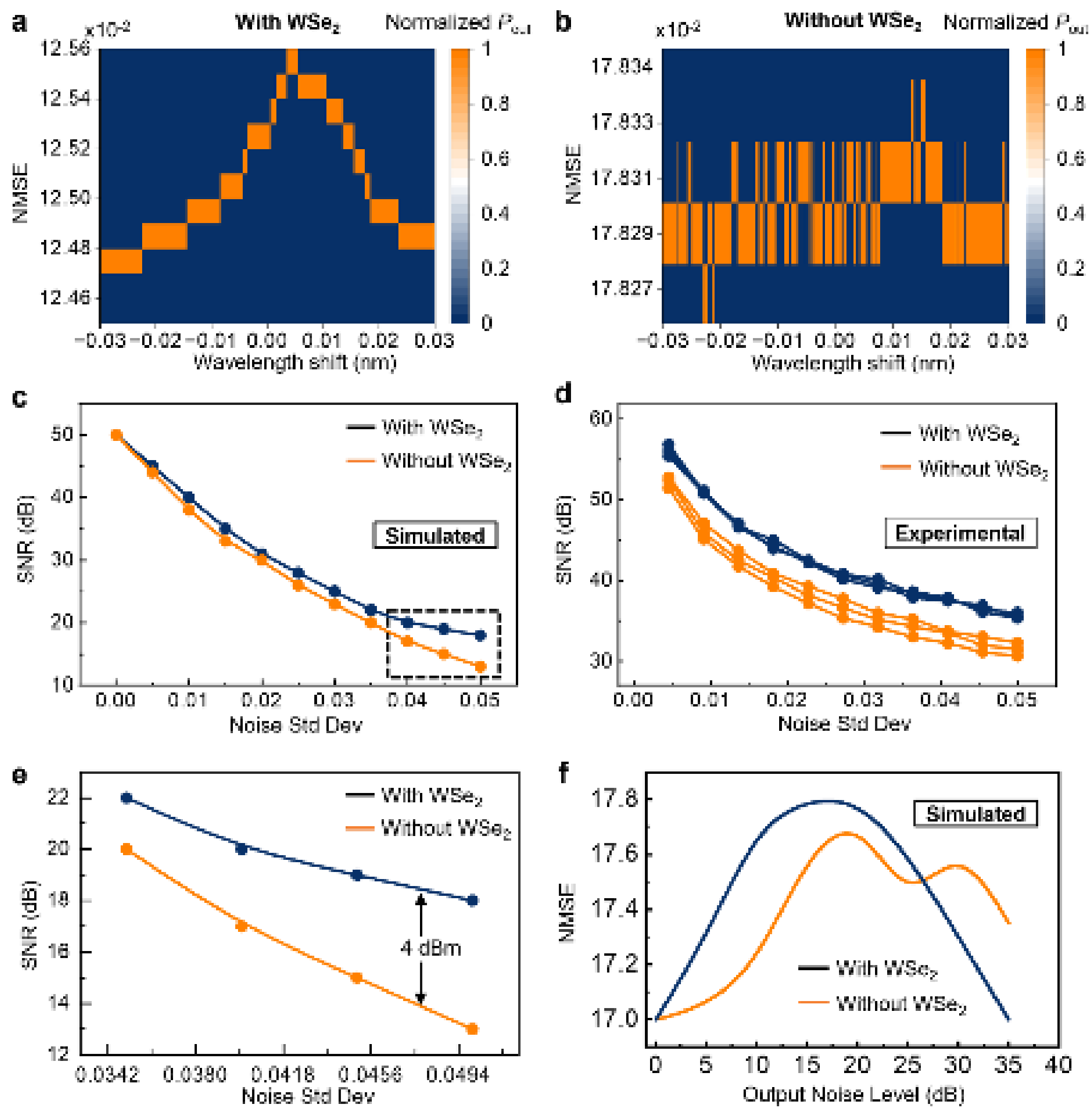

Figure 3. Noise robustness of SiN microring photonic reservoirs with and without 2D-material integration. Normalized mean-squared error (NMSE) as a function of wavelength detuning for reservoirs (a) with a WSe_2 layer and (b) for bare SiN devices. The 2D-integrated resonator exhibits a stable and symmetric NMSE. (c) Simulated signal-to-noise ratio (SNR) versus input noise standard deviation, showing consistently higher SNR for the 2D-integrated reservoir across noise levels. (d) Experimental SNR measurements confirm the simulations: the WSe_2-coated resonator maintains superior SNR over the entire range. (e) Magnified high-noise regime from simulations, highlighting an average SNR gain of ~4 dB with 2D integration. (f) NMSE versus output noise level, where the 2D-enhanced reservoir achieves lower and smoother NMSE than the bare device, evidencing improved noise tolerance and computational stability.

Figure 3 quantitatively compares the computational accuracy and stability of the reservoir with and without the WSe_2 layer. To evaluate the impact of the added nonlinearity and bistability, we calculated the normalized mean-square error (NMSE) and signal-to-noise ratio (SNR) for both configurations, highlighting the improved efficiency and noise resilience achieved with WSe_2 integration. The SiN microring reservoir integrated with WSe_2 exhibits a symmetric and narrow NMSE distribution, indicating stable resonance and consistent prediction, shown in figure 3a. A well-defined ridge near zero detuning and a low NMSE (~0.1247), confirm a robust operating point with minimal drift. In contrast, the bare SiN device shows irregular, NMSE (~0.1782) features over detuning range, reflecting weak nonlinearity and resonance instability that degrade prediction accuracy, figure 3b. NMSE is calculated using equation (1).

$$\mathrm{NMSE} = \frac{\sigma_n^2}{\frac{1}{N}\sum_{i=1}^{N} x_i^2}\ ,\ \sigma_n = \sqrt{\frac{1}{N}\sum_{i=1}^{N}(x_i - \bar{x})^2} \quad \ldots..\ (1)$$

While doing the simulations, zero-mean Gaussian noise with increasing standard deviation is introduced to evaluate the stability. The SNR decreases with higher noise levels, yet the WSe_2-integrated device remains consistently higher than the control across the sweep, Figure 3c. SNR (dBm) is calculated using equation (2). The separation between SNR values of the two, with and without 2D material integration, becomes especially pronounced in the high-noise regime, where the WSe_2 device gains an advantage of approximately 4 dB, as highlighted in the magnified view in Figure 3e.

$$\mathrm{SNR} = 10\log_{10}^{\left(\frac{P_{\mathrm{signal}}}{P_{\mathrm{noise}}}\right)} \quad \ldots.\ (2)$$

Experimental measurements (Figure 3d) show a consistent trend with the simulations. For equivalent noise levels, the WSe_2-integrated microring exhibits a systematically higher SNR than the bare SiN device, confirming that the inclusion of the 2D layer enhances noise tolerance and stabilizes the reservoir's dynamic response in practice. Figure 3f plots the NMSE against output-noise level and reveals a characteristic non-monotonic, hump-shaped dependence for both devices, often associated with stochastic-resonance, where the error rises from a low-noise floor, peaks at an intermediate noise level, and then falls at higher noise. The WSe_2 device peaks at a slightly higher noise level and maintains lower NMSE at both the low and high noise extremes, indicating a broader, more forgiving operating window and greater computational robustness. This shows that integrating WSe_2 yields a smoother response, a consistent several-decibel SNR advantage under injected Gaussian noise (with ~4 dB at high noise), and improved retention of low NMSE across noise conditions.

Aspect	**This work**	**Donati et al.** [26]	**Zhao et al.**[21]	**Castro et al.**[1]	**Ren et al.** [32]
Platform	SiN + WSe_2 microring	Si microring + delayed feedback	SiN microring only	Si microring	Si microring + series-coupled linear cavities
NMSE	0.12	~0.18–0.22	~0.16–0.18	~0.17–0.19	~0.15
SNR	Improved by ~4 dB	Not improved	No improvement	Not improved	Not reported / similar
Study of noise	Device engineered for noise robustness	Studies degradation due to noise	No explicit noise study	Studies cavity nonlinearities & loss	Focus on memory capacity, not noise

Table 1. Comparison of NMSE and noise performance across different MRR-based photonic reservoir platforms.

The table provides a comparative evaluation of our WSe_2-SiN microring reservoir against four representative photonic reservoir computing architectures reported in prior literature. While all reference systems rely solely on silicon or SiN microring with performance shaped by intrinsic free-carrier or thermo-optic nonlinearities our device uniquely integrates a 2D material to strengthen the nonlinear response and stabilize resonance behavior under noise. As a result, our system achieves lower prediction error (NMSE ≈ 0.12) and an SNR improvement of approximately 4 dB, outperforming silicon microring reservoirs with delayed feedback, SiN microring systems lacking external enhancement[21],and silicon microring implementations dominated by cavity losses. Although Ren et al.'s architecture enhances memory capacity through multiple coupled linear cavities, it does not address noise robustness and achieves a higher error (~0.15) despite substantially greater structural complexity[32]. Overall, the comparison highlights that our WSe_2-SiN microring reservoir can be the solution for noise resilience, offering improved NMSE and SNR without requiring long delay lines or cascaded cavity arrays.

Time series prediction using photonic RC and validation with NARMA10 &20

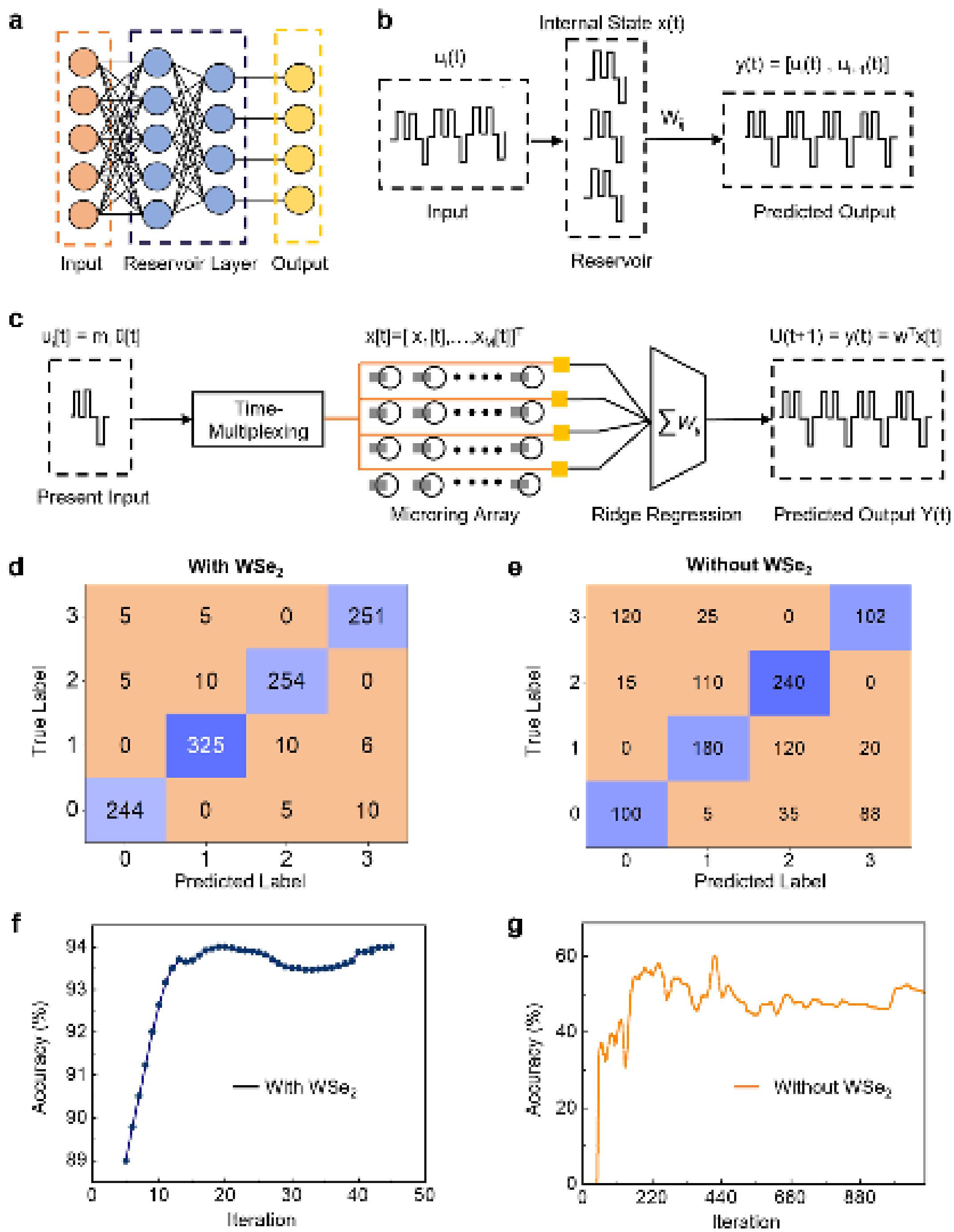

Figure 4. Comparison analysis of Time Series Prediction with SiN microring with WSe_2 and without WSe_2. (a) Conceptual view of the learning paradigm showing the input layer, the reservoir layer and the output layer. (b) Schematic diagram of Photonic-reservoir implementation of time-series prediction. (c) Detailed schematic of time series prediction in photonic reservoir computing. (d) Confusion matrix for the WSe_2 integrated SiN microring reservoir on a time-series prediction task. (e) Confusion matrix for the bare SiN reservoir under identical conditions.

(f) Iteration test accuracy for the WSe_2-integrated reservoir. Accuracy rises steadily with iteration and plateaus above 90%, showing smooth convergence and low run-to-run variability. (g) Iteration test accuracy for the bare SiN reservoir. Accuracy remains less than 50 % for same number of iteration but reaches to 60% after 200 iterations.

Time-series prediction is a key application of reservoir computing. Here we used it to demonstrate how the proposed WSe_2-SiN reservoir maintains stable and predictable dynamics under noise, showcasing its enhanced robustness for real-world signal processing tasks. The reservoir should be stable, predictable, and robust to noise. Figure 4a shows a schematic of the standard RC topology: an input stream feeds a high-dimensional recurrent reservoir, which transforms the input into a rich internal state. A linear readout is then trained to map these states to the target output, with only the output weights being trained, keeping learning fast and data efficient. In time-series prediction, the input u(t) is the present signal, and the goal is to predict u(t+1), the future signal, by learning patterns from past and present inputs. This setup also allows us to study how noise affects the reservoir computer.

In temporal processing, Figure 4b zooms into the time-domain flow. At each time step t, an input segment $u_k(t)$ (left) is injected into the physical reservoir. The reservoir dynamics produce an internal state vector x(t) (center). A linear combiner with weights W_{ij} forms the predicted output y(t) = u(t+1) (right). Conceptually, the reservoir expands the input into a nonlinear, memory-bearing feature space. The readout then performs a simple ridge regression in that space.

RC implementation on the device level is one of the best advantages. Figure 4c gives a description of the time series prediction on the photonic device level implementation. In the input $u_i(t)$ is the present signal. Each scalar input sample u[t] is encoded as an optical intensity waveform and stretched over a symbol window of duration T.

$$\tilde{u}(t) = \frac{u(t)-u_{min}}{u_{max}-u_{min}} \quad \ldots\ldots (3)$$

This time-multiplexing creates M "virtual nodes" per input without adding hardware: the masked slices $u_i(t) = m_i\, \tilde{u}(t)$, where m_i is the mask. In our hardware, each slice drives an array of microring resonators (MRRs) that are DC-biased close to resonance, so small intensity changes translate into significant phase/transfer changes at the output port. An MRR provides both nonlinearity and short-term memory. Then time index t (in samples), define node i ∈ {1, …M}. Discretized at the slot rate, this yields a leaky state update of the form, $x_i(t)=f\,(m_i.\ \tilde{u}(t-(M-i)\ s))$, where f(.) is a nonlinearity (e.g., tanh or ReLU). The output transmission is sampled once per sub-slot to form the state vector $x(t) = [x_i(t)\dots x_M(t)]^T$. Training is performed only at the readout. State vectors collected over T_{train} steps are assembled into a matrix X, paired with targets y(t) and a ridge-regression solution is computed:

$$W= (x^T x +\lambda I)^{-1} x^T y \quad \dots. (4)$$

During inference, outputs are produced by the linear projection $y(t) = W^T x(t)$.

Adding WSe_2 enhances the ring's nonlinearity and reduces excess noise by improving the balance of its internal dynamics. Future prediction accuracy is summarized in Figures 4d and 4e using confusion matrices. With WSe_2, a tight diagonal clustering of counts is observed, indicating that most samples are correctly classified; off-diagonal entries remain sparse and small, yielding 94% accuracy. Without WSe_2, the diagonal is weaker and larger off-diagonal blocks appear, indicating more frequent misclassifications and degraded class separability, with accuracy reduced to 60%. Consistent with this, the WSe_2 reservoir produces cleaner, more discriminative state-space embeddings. Figures 4f and 4g show accuracy versus iteration: to approach 94% accuracy, the device without WSe_2 requires more than 8000 iterations, whereas the WSe_2-integrated device reaches this accuracy within about 40 iterations.

To further evaluate the performance of the proposed WSe_2-SiN reservoir, we employed the NARMA-10 and NARMA-20 tasks. NARMA is a standard nonlinear time series bench mark that test how well reservoir computing system can handle both memory and nonlinear relationship[3]. NARMA-10 means future prediction depends upon past 10 inputs, similarly for NARMA-20 future prediction depends upon 20 past inputs [3,32]. Equation (5) and equation (6) shows NARMA-10 and NARMA-20.

NARMA-10: $y(t) = 0.3y(t) + 0.05\, y(t)[\sum_{i=0}^{9} y(t-i)] + 1.5\, u(t-9)\, u(t) + 0.1 \dots\dots (5)$

NARMA-20: $y(t) = 0.3y(t) + 0.05\, y(t)[\sum_{i=0}^{19} y(t-i)] + 1.5\, u(t-19)\, u(t) + 0.1 \dots.\ (6)$

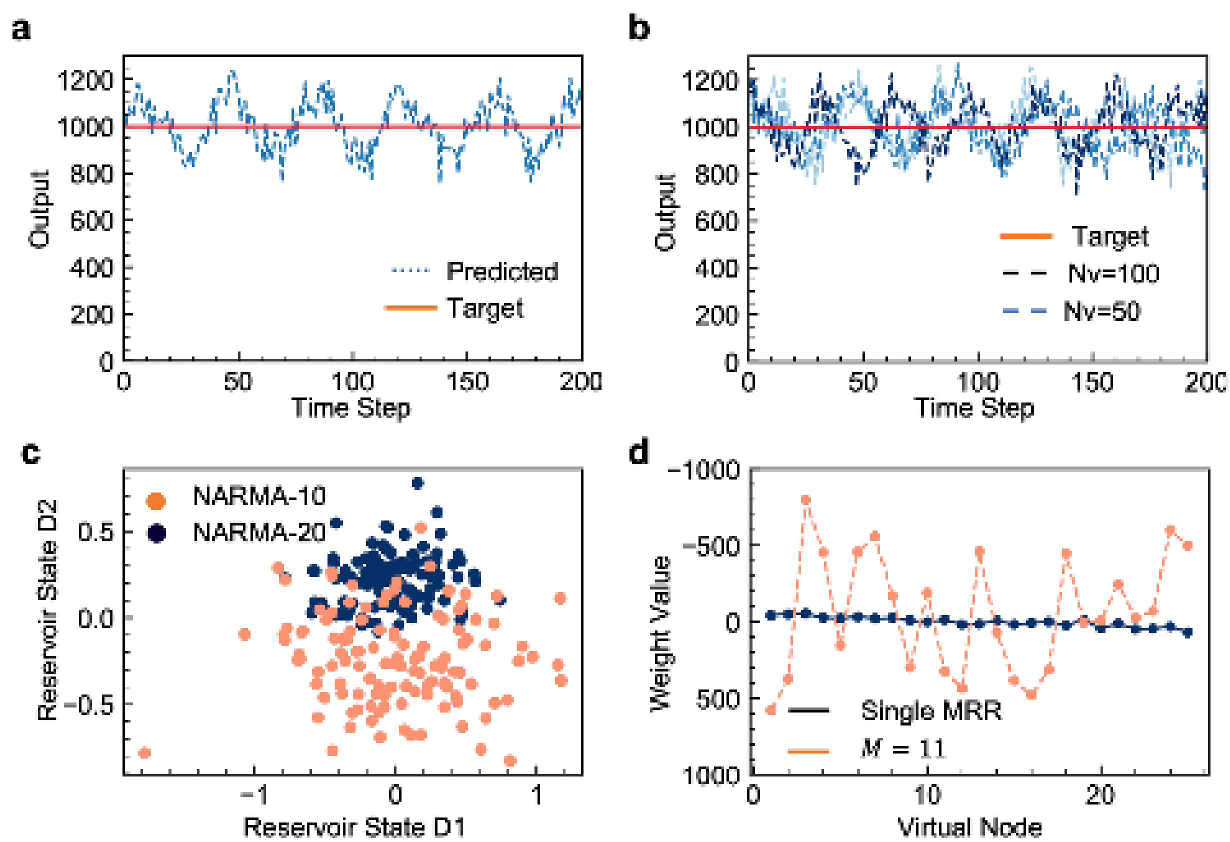

Figure 5. Benchmark for SiN microring photonic reservoir computing system. (a) Predicted versus target output for the NARMA-10 time-series task, showing accurate temporal tracking with low normalized mean squared error (NMSE). (b) Comparison of predicted outputs for different numbers of virtual nodes, where increasing node count enhances memory capacity and prediction stability. (c) Two-dimensional projection of simulated reservoir states for NARMA-10 and NARMA-20 tasks. (d) Distribution of trained readout weights across virtual nodes for the simulated 2D-integrated microring resonator (M = 11).

In Figure 5a, the system's ability to track a nonlinear dynamical process is shown using the NARMA-10 benchmark, a canonical test that demands both nonlinearity and long temporal memory. The target sequence (solid line) and the reservoir's prediction (dotted line) are plotted versus time step. The close overlay of the two traces across peaks, troughs, and plateaus indicates faithful temporal tracking with a low normalized mean-squared error (NMSE). Deviations remain small, implying that the readout has extracted a sufficiently rich, history-dependent feature set from the ring dynamics to reconstruct the output without overfitting. Figure 5b examines how the number of virtual nodes Nv influences prediction stability. Two predicted outputs are compared against the same target: one with Nv = 50 and another with Nv = 100. Increasing the node count clearly tightens the fit. The Nv =100 curve (dark dashed) hugs the target more closely than the Nv =50 curve (light dashed), demonstrating the standard reservoir-computing trade-off: more nodes enlarge the adequate state space and memory capacity, enabling finer separation of temporal features at the readout. In practice, boosting Nv improves noise averaging, reduces jitter, and mitigates underfitting, all of which are reflected here as smaller residuals relative to the ground truth. To visualize how the physical dynamics encode inputs, Figure 5c projects the high-dimensional reservoir states onto two principal axes ("Reservoir State D1" and "Reservoir State D2"). Two datasets are shown: NARMA-10 (orange) and the harder NARMA-20 (blue), which requires substantially longer memory. Distinct, well-separated clusters are obtained: the NARMA-20 points concentrate in a compact region while the NARMA-10 points populate a different area with minimal overlap. Such separation implies that the internal microring responses map the two tasks to discriminable manifolds, easing the burden on the linear readout. The clear clustering is consistent with enhanced χ^3 nonlinearity supplied by the 2D material overlay, which steepens the effective transfer function and enriches state diversity without sacrificing stability.

Figure 5d, plots the trained readout weights assigned to each virtual node (horizontal axis) for two conditions: a single-MRR baseline (dark markers) and a simulated 2D-integrated microring characterized by M=11 nodes (peach, dashed). The baseline weights remain small and narrowly distributed around zero, signaling limited expressiveness in the features produced by the plain ring. In contrast, the 2D-enhanced case yields a broad, asymmetric spread spanning large positive and negative values, indicating that the readout relies on more varied and informative components of the state vector. This broader utilization is a hallmark of stronger nonlinearity and higher computational richness: the reservoir provides diverse basis functions over time, and the linear combiner exploits them to reconstruct complex outputs. On-chip deployment of photonic reservoir computing is mainly challenged by scalable 2D-material integration, device reproducibility, thermal control, and system-level integration, with fabrication variability causing performance fluctuations. From a manufacturing standpoint, compatibility with CMOS foundry processes, yield, and integration density will be critical to transitioning reservoir architectures from laboratory demonstrations to larger-scale implementations.

Conclusion

In this work, we tackle the problem of noise-induced instability in reservoir computing with a hybrid WSe_2–SiN MRR platform. This work combines the low optical loss and thermal stability of SiN with the strong nonlinear response of WSe_2, effectively suppressing resonance drift and spontaneous switching without additional feedback control. Both simulations and experiments confirm a 4 dB increase in SNR, a 30% reduction in NMSE, and faster training convergence on NARMA benchmarks, achieving ~94% prediction accuracy within 30–40 iterations. Further performance improvements can be achieved by integrating materials with even higher χ^3, provided they introduce minimal optical absorption and waveguide loss. These results establish the WSe_2–SiN microring as a robust, energy-efficient reservoir computing node that supports long-term stability, offering a scalable route toward noise-tolerant photonic processors for high-speed signal prediction and edge-AI applications.

Methodology

SiN waveguide fabrication: Commercially available SiN-on-SiO_2 wafers with a 350-nm silicon nitride layer on a thermally oxidized substrate were used for device fabrication. Electron-beam lithography (Raith 100 kV) with ARP 6200 resist was employed to define the waveguide patterns. After development, the features were transferred into the SiN layer using inductively coupled plasma reactive ion etching with CHF_4 as the primary etchant and a controlled Ar co-flow to stabilize the etch rate and chamber pressure. The residual resist was removed by oxygen plasma ashing. Finally, a short oxygen plasma treatment was performed to render the surface hydrophilic and facilitate van der Waals integration of the 2D flakes.

Mode simulation: Numerical simulations of the microring resonator were performed using Lumerical FDTD and FDE solvers. The model consisted of a microring side-coupled to a straight bus waveguide, with material parameters chosen to match experimental conditions. Perfectly matched layer boundaries were applied to suppress reflections from the simulation edges. A broadband optical source was launched into the bus waveguide to excite resonant modes, and field monitors were positioned along the structure to capture the electromagnetic field distribution. To improve numerical precision, especially at the coupling region and the WSe_2-ring interface, a refined, non-uniform mesh was employed. From the recorded data key parameters like resonance wavelength, quality factor, and free spectral range is noted.

Time series simulation: To assess the WSe_2-SiN platform, we measured a single physical node and created M virtual nodes via time-multiplexing by masking the input sequence and feeding the M slices sequentially within a single symbol. A reference time series was generated (Equation 3), and the transmission through output port was sampled once per sub-slot to form an M-dimensional state vector. Training was readout-only: state vectors were stacked and paired with targets to obtain ridge-regression weights (Equation 4). In inference, outputs were the linear projection of the current state for one-step-ahead prediction u(t+1). Performance was evaluated on NARMA-10 and NARMA-20 (Equations 5-6) to quantify nonlinear memory and predictive capability.

Acknowledgements

This work is supported by the Singapore Ministry of Education (MOE) Academic Research Fund (AcRF) Tier 1 grants (RG63/23, RT2/23, RG71/25), Tier 2 (MOE-T2EP50224-0018), and Tier 3 grant (MOE-MOET32023-0003) "Quantum Geometric Advantage". This work is also supported in part by Agency for Science, Technology and Research (A*STAR) under its MTC Programmatic Grant (M23M2b0056). S.H.C. acknowledges funding from the A*STAR, Singapore, Advanced Manufacturing and Engineering (AME) Individual Research Grant (IRG) under the Project M23M6c0109. This work was also supported by the ANR (French National Research Agency) project MILPHEUILLE (ANR-25-CE09-2554) and PHC Merlion programme (51272YD), funded by the French Ministry for Europe and Foreign Affairs, the French Ministry for Higher Education and Research, and Nanyang Technological University. The authors acknowledge the support of the Nanyang NanoFabrication Centre (N2FC). AFM measurements were performed using Park Systems Park NX10 model.

Conflict of Interest

The authors declare no conflict of interest.

Data Availability Statement

The data that support the findings of this study are available from the corresponding author upon reasonable request.

References:

1. Castro, B. J. G., Peucheret, C., Zibar, D. & Ros, F. D. Effects of cavity nonlinearities and linear losses on silicon microring-based reservoir computing. *Opt. Express* **32**, 2039 (2024).
2. Duport, F., Schneider, B., Smerieri, A., Haelterman, M. & Massar, S. All-optical reservoir computing. *Opt. Express* **20**, 22783 (2012).
3. Donati, G., Mirasso, C. R., Mancinelli, M., Pavesi, L. & Argyris, A. Microring resonators with external optical feedback for time delay reservoir computing. *Opt. Express* **30**, 522 (2022).
4. Borghi, M., Biasi, S. & Pavesi, L. Reservoir computing based on a silicon microring and time multiplexing for binary and analog operations. *Sci. Rep.* **11**, 15642 (2021).
5. Farmakidis, N., Dong, B. & Bhaskaran, H. Integrated photonic neuromorphic computing: opportunities and challenges. *Nat. Rev. Electr. Eng.* **1**, 358–373 (2024).
6. Kanno, K., Naruse, M. & Uchida, A. Adaptive model selection in photonic reservoir computing by reinforcement learning. *Sci. Rep.* **10**, 10062 (2020).
7. Moon, J. *et al.* Temporal data classification and forecasting using a memristor-based reservoir computing system. *Nat. Electron.* **2**, 480–487 (2019).
8. Wang, D., Nie, Y., Hu, G., Tsang, H. K. & Huang, C. Ultrafast silicon photonic reservoir computing engine delivering over 200 TOPS. *Nat. Commun.* **15**, 10841 (2024).
9. Vandoorne, K. *et al.* Experimental demonstration of reservoir computing on a silicon photonics chip. *Nat. Commun.* **5**, 3541 (2014).
10. Wang, T. *et al.* Reservoir Computing and Task Performing through Using High-β Lasers with Delayed Optical Feedback. *Prog. Electromagn. Res.* **178**, 1–12 (2023).
11. Yeminy, T., Sadot, D. & Zalevsky, Z. Analysis of photonic noise generated due to Kerr nonlinearity in silicon ring resonators. *Opt. Express* **26**, 284 (2018).
12. Inubushi, M. & Yoshimura, K. Reservoir Computing Beyond Memory-Nonlinearity Trade-off. *Sci. Rep.* **7**, 10199 (2017).
13. Cheng, T.-Y., Liu, C.-C., Jhou, D.-Y. & Chen, C.-C. Impact of coupling topology upon noise robustness of small optical reservoirs. *Sci. Rep.* **10**, 14086 (2020).

14. Borghi, M., Bazzanella, D., Mancinelli, M. & Pavesi, L. On the modeling of thermal and free carrier nonlinearities in silicon-on-insulator microring resonators. *Opt. Express* **29**, 4363 (2021).
15. Novarese, M. *et al.* Study of nonlinear effects and self-heating in a silicon microring resonator including a Shockley-Read-Hall model for carrier recombination. *Opt. Express* **30**, 14341 (2022).
16. Tritschler, P. *et al.* Nonlinear Optical Bistability in Microring Resonators for Enhanced Phase Sensing. *Phys. Rev. Lett.* **134**, 123802 (2025).
17. Alharbi, G., Gong, Y., Wong, S. & Oh, S. S. Bistability in Photonic Topological Insulators with Kerr Nonlinearity. in *Conference on Lasers and Electro-Optics* JTh3A.69 (Optica Publishing Group, San Jose, California, 2021). doi:10.1364/CLEO_AT.2021.JTh3A.69.
18. Arbabi, A., Lu, P.-K., Griffin, B. G. & Goddard, L. L. Thermally-induced nonlinearity and optical bistability in Si3N4 microring resonators. in *Conference on Lasers and Electro-Optics 2012* JW4A.90 (OSA, San Jose, California, 2012). doi:10.1364/CLEO_AT.2012.JW4A.90.
19. Priem, G. *et al.* Optical bistability and pulsating behaviour in Silicon-On-Insulator ring resonator structures. *Opt. Express* **13**, 9623 (2005).
20. Wang, C.-T. *et al.* Optical bistability in a silicon nitride microring resonator with azo dye-doped liquid crystal as cladding material. *Opt. Express* **21**, 10989 (2013).
21. Zhao, L. *et al.* Integrated silicon-photonic reservoir computing with an on-chip Si3N4 microcavity. *Opt. Commun.* **591**, 132133 (2025).
22. Cui, Q., Muniz, R. A., Sipe, J. E. & Zhao, H. Strong and anisotropic third-harmonic generation in monolayer and multilayer ReS 2. *Phys. Rev. B* **95**, 165406 (2017).
23. Wei, G., Stanev, T. K., Czaplewski, D. A., Jung, I. W. & Stern, N. P. Silicon-nitride photonic circuits interfaced with monolayer MoS2. *Appl. Phys. Lett.* **107**, 091112 (2015).
24. Hendry, E., Hale, P. J., Moger, J., Savchenko, A. K. & Mikhailov, S. A. Coherent Nonlinear Optical Response of Graphene. *Phys. Rev. Lett.* **105**, 097401 (2010).
25. Zhou, C. *et al.* Photonic deep residual time-delay reservoir computing. *Neural Netw.* **179**, 106575 (2024).
26. Donati, G., Argyris, A., Mirasso, C. R., Mancinelli, M. & Pavesi, L. Noise effects on time delay reservoir computing using silicon microring resonators. in *Integrated Optics: Devices,*

Materials, and Technologies XXVI (eds García-Blanco, S. M. & Cheben, P.) 55 (SPIE, San Francisco, United States, 2022). doi:10.1117/12.2609056.

27. Wang, Y. *et al.* Enhancing $Si_3 N_4$ Waveguide Nonlinearity with Heterogeneous Integration of Few-Layer WS_2. *ACS Photonics* **8**, 2713–2721 (2021).
28. Basyooni, M. A., Zaki, S. E., Tihtih, M., Eker, Y. R. & Ateş, Ş. Photonic bandgap engineering in $(VO_2)_n/(WSe_2)_n$ photonic superlattice for versatile near- and mid-infrared phase transition applications. *J. Phys. Condens. Matter* **34**, 325901 (2022).
29. Gao, Y., Zhou, W., Sun, X., Tsang, H. K. & Shu, C. Cavity-enhanced thermo-optic bistability and hysteresis in a graphene-on-Si_3N_4 ring resonator. *Opt. Lett.* **42**, 1950 (2017).
30. Zhang, L. *et al.* Multibistability and self-pulsation in nonlinear high- Q silicon microring resonators considering thermo-optical effect. *Phys. Rev. A* **87**, 053805 (2013).
31. Wang, J. *et al.* Optical bistability in a silicon nitride microring integrated with 2D PtSe2 [Invited]. *Chin. Opt. Lett.* **22**, 091301 (2024).
32. Ren, H. *et al.* Photonic time-delayed reservoir computing based on series-coupled microring resonators with high memory capacity. *Opt. Express* **32**, 11202 (2024).